TU Delft

Delft University of Technology

Vortex merging in a laminar separation bubble under natural and forced conditions

Kurelek, J. W.; Yarusevych, S.; Kotsonis, M.

DOI
10.1103/PhysRevFluids.4.063903

Publication date
2019

Document Version
Accepted author manuscript

Published in
Physical Review Fluids

Citation (APA)
Kurelek, J. W., Yarusevych, S., & Kotsonis, M. (2019). Vortex merging in a laminar separation bubble under natural and forced conditions. *Physical Review Fluids*, *4*(6), Article 063903. https://doi.org/10.1103/PhysRevFluids.4.063903

Important note
To cite this publication, please use the final published version (if applicable).
Please check the document version above.

Copyright
Other than for strictly personal use, it is not permitted to download, forward or distribute the text or part of it, without the consent of the author(s) and/or copyright holder(s), unless the work is under an open content license such as Creative Commons.

Takedown policy
Please contact us and provide details if you believe this document breaches copyrights.
We will remove access to the work immediately and investigate your claim.

This work is downloaded from Delft University of Technology.
For technical reasons the number of authors shown on this cover page is limited to a maximum of 10.

Vortex merging in a laminar separation bubble under natural and forced conditions

J. W. Kurelek and S. Yarusevych*

Department of Mechanical and Mechatronics Engineering, University of Waterloo, Waterloo, Ontario, Canada N2L 3G1

M. Kotsonis†

Faculty of Aerospace Engineering, Delft University of Technology, Delft 2629HS, The Netherlands

(Dated: August 5, 2019)

Vortex merging in a laminar separation bubble (LSB) is studied experimentally. The bubble is formed on the suction side of a NACA 0018 airfoil at an angle of attack of 4° and a Reynolds number of 125 000. The merging process in the bubble is manipulated through acoustic forcing applied as a tone at either the fundamental vortex shedding frequency or at the first subharmonic of this frequency. The flow field is assessed using time-resolved, two-component particle image velocimetry. A method for detecting merged structures using wavelet analysis is introduced, allowing for reliable quantification of merging events. The results show that vortex merging occurs naturally in the separation bubble, while forcing at the subharmonic and fundamental frequencies promotes and inhibits merging, respectively. While these trends are similar to those observed for free shear layers, the subharmonic forcing of an LSB is found to directly promote disturbance development at the subharmonic frequency. For all cases, the majority of merging events take place in the aft portion of the bubble, i.e., downstream from the maximum bubble height location and upstream of mean reattachment, with subharmonic forcing causing merging to shift upstream. The merged structures are found to be the most energetic flow features, however, promoting vortex merging through subharmonic forcing does not lead to significant changes in the mean bubble topology. The spanwise behavior of the vortex merging process is studied, revealing that structures merge in a spanwise non-uniform manner, with localized merging occurring away from where forward or rearward streamwise bugles develop in the vortex filaments. Statistical characterization reveals that merging tends to occur more often over some specific spanwise segments, with the number of primary structures that merge varying by as much as 50% between spanwise locations. These findings offer insight into vortex merging in laminar separation bubbles and the attendant influence of forcing, while also highlighting the need to consider spanwise aspects of flow development.

* syarus@uwaterloo.ca
† m.kotsonis@tudelft.nl

I. INTRODUCTION

A laminar separation bubble can form on a lifting surface if the boundary layer is initially laminar and subjected to a sufficiently strong adverse pressure gradient, causing flow separation. A separated shear layer with an inflectional velocity profile is formed, where accelerated laminar-to-turbulent transition occurs. As the flow transitions, the entrainment of momentum from the outer-flow to the near-wall region is enhanced and, depending on the flow conditions and geometry of the surface, the flow can reattach in a mean sense and form an LSB. This description of LSB mean topology originates from the seminal works summarized by Tani [1], followed by those of Gaster [2] and Horton [3], and has required little revision over the years [4, 5].

LSB formation is common for aerodynamic bodies operating at low chord-based Reynolds numbers ($Re_c \lesssim 10^6$), such as those employed in glider and unmanned aerial vehicles [6] and aircraft turbofan engines in cruise [7]. For these applications, LSB formation often leads to undesirable effects, including loss of lift, increase in drag, and noise emissions [8, 9]. In an effort to mitigate these undesirable effects, recent research efforts have been focused on the laminar-to-turbulent transition process within the LSB so that, ultimately, the underlying physics may be understood and effective control strategies developed. To this end, much progress has been made in the last several decades toward understanding the initial stage of LSB transition [10], namely, in the fore portion of the bubble where disturbance amplitudes are small. The initial conditions for the transition process are set by small amplitude disturbances present within the upstream attached boundary layer [11–14]. These disturbances convect into the fore portion of the bubble, where the flow is essentially two-dimensional and parallel, and so many investigators have found this initial stage of transition to be well modeled by linear stability theory [12, 15–17], finding that disturbance growth is primarily due to an inviscid Kelvin-Helmholtz-type instability. This view of the transition process has become well accepted among the research community as a result of the excellent agreement between experimental and numerical results with stability predictions [18–21], with similarities to free shear layers noted [22].

A common feature of laminar-to-turbulent transition in shear flows, e.g., boundary layers [23], separated shear layers formed on bluff bodies [24], and free shear layers [25], is the formation of coherent structures that precede the production of small-scale turbulence. The most prominent coherent structures formed during shear flow transition are elongated and two-dimensional spanwise-oriented vortices. Ho and Huerre [25] attribute the formation of such structures in free shear flows to the continued growth of the Kelvin-Helmholtz instability wave, leading to its saturation and the rise of harmonics and subharmonics. Consecutive and spanwise-uniform vortices connected via thin filaments form, with the process roughly completed at the location where the growth of the main instability wave saturates. A similar process is observed in separation bubbles, regardless of whether the bubble is formed over a flat plate subjected to an adverse pressure gradient or an airfoil [22, 26–30]. Continued disturbance growth in the separation bubble eventually leads to nonlinear wave interactions, followed by shear layer roll up and quasiperiodic vortex shedding in the aft portion. These structures dominate the flow development [31, 32] and have been argued to be responsible for inducing mean reattachment [33, 34]. At formation, the vortices have been described as spanwise uniform [35–38] or highly deformed and arranged in a staggered pattern [26, 39, 40], with the differences attributed to the relative amplitudes of the main Kelvin-Helmholtz instability and any oblique disturbance modes which may be active [41]. Regardless, the structures undergo further three-dimensional deformations due to the onset of secondary instabilities [27, 29], followed by the breakdown to turbulence.

Vortex merging is an intrinsic process to shear flows, where the pairing of consecutive, co-

rotating vortices has been shown to plays a major role in the decay of turbulence [42–45] and in the growth of and momentum transfer across mixing layers [25, 46]. According to Hopfinger and van Heijst [47], the process of vortex merging is the predominant mechanism for the evolution of decaying turbulence, and hence has been studied extensively. The fundamental aspects of vortex merging have been investigated by Cerretelli and Williamson [48] and Meunier *et al.* [49], with the initial stage of merging involving two vortices undergoing diffusive growth while orbiting one another. When the size of the vortex cores exceeds a critical proportion of the vortex spacing, the vortex centroids begin to approach each other. The cores eventually merge, forming a single merged vorticity structure that continues to expand through diffusion. In regard to free shear layers, this process has been captured and studied in numerous investigations, summarized in the review of Ho and Huerre [25]. Through consecutive merging of vortex pairs, the vorticity contained within each structure is constantly redistributed into increasingly larger vortices, resulting in an approximate doubling of their wavelength and strength after each merge, while their characteristic frequency is halved [50]. In contrast to free shear layers, while similar vortex merging has been observed in separation bubbles [36–38], the number of studies is limited and observations have been largely cursory and/or qualitative. A noted exception is the investigation of Lambert and Yarusevych [38], who studied the associated vortex dynamics through simultaneous time-resolved flow visualizations and surface pressure measurements. For a separation bubble formed over a NACA 0018 airfoil at a chord Reynolds number of 100 000 and an angle of attack of 8°, they found up to 15% of vortices in the suction side LSB merge, with merging events occurring primarily upstream of the mean reattachment location and in an aperiodic fashion.

Much insight into the transition process and the ensuing vortex dynamics of LSBs has been gained through investigations that affect flow development through the introduction of controlled periodic disturbances. This type of forcing has been introduced in experimental and numerical studies by various means, including wall oscillations [18, 51, 52], external acoustic excitation [53], and wall-mounted plasma actuators [21, 34]. The sensitivity of the LSB to periodic forcing has also been explored for flow control purposes aimed at stall control and improvement of airfoil performance at prestall conditions, e.g., using synthetic jets [54, 55] and external acoustic excitation [56–58]. Several investigators have linked the optimal excitation frequency to that of the most amplified disturbances in the natural flow [20, 59], showing that inducing flow reattachment on a stalled airfoil through the formation of an LSB or reducing the size of an existing LSB is most effective when the excitation frequency targets the natural Kelvin-Helmholtz instability and the associated vortex shedding process. It has been demonstrated that forcing at this "fundamental" frequency has a significant impact on the ensuing vortex dynamics [34, 60]; as the shedding process locks to the excitation frequency, vortex formation occurs further upstream and the coherence of the structures is increased. This has been shown to have significant influence over the mean separation bubble topology [33, 34], with the upstream advancement of vortex formation being the most significant factor influencing the mean reattachment location [60].

While the problem of forcing an LSB at its fundamental frequency has been studied extensively, the effects of forcing at subharmonic frequencies on LSB flow development and vortex merging remain relatively unknown, as a detailed examination has yet to be conducted. Such an investigation has merit since, in the case of free shear flows, subharmonic forcing has been shown to have significant influence over the vortex dynamics, specifically through manipulation of the vortex merging process. In particular, applying external acoustic forcing at or near the fundamental frequency synchronizes the initial roll-up process, creating a well defined maximum in the fundamental perturbation energy at the streamwise roll-up location, at which point the subharmonic component begins to grow, reaching a maximum at a pairing location further downstream

(Fig. 3 in Ref. 25). However, forcing in the vicinity of the fundamental frequency inhibits pairing with respect to the natural case [61]. Ho and Huang [62] showed that the process can be manipulated by altering the forcing frequency, as after disturbance growth at the fundamental frequency saturates, a secondary subharmonic resonance mechanism gives rise to subharmonic disturbance growth [63, 64]. Thus forcing applied at the first subharmonic frequency accelerates the growth of the subharmonic mode, which was found to promote vortex pairing and increase the rate of momentum transfer across the layer, relative to the unforced case [62]. Similar to the roll-up location coinciding with the peak in the fundamental mode, the pairing location occurs downstream where the subharmonic mode reaches a maximum [62].

Despite playing a major role in the development of free shear flows, there is a lack of insight into the role of vortex merging in laminar separation bubble dynamics. It remains to be determined if vortex merging has significant effect on LSB mean topology, through influence of the reattachment process or otherwise, and whether merging can be manipulated via forcing to the same effect as seen in free shear layers. It is the goal of the present investigation to answer these questions through examination of the spatiotemporal evolution and merging characteristics of coherent structures within an LSB. The flow is forced using external acoustic excitation applied as a tone at either the fundamental or subharmonic frequency. Measurements are performed using time-resolved, two-component particle image velocimetry (PIV) in two spatial orientations, allowing for cross-examination of the vortex dynamics and mean topological features of the bubble.

II. EXPERIMENTAL SETUP

Experiments were conducted in a recirculating wind tunnel at the University of Waterloo. The tunnel test section is 2.44 m long, 0.61×0.61 m in cross section, and features full optical access. The tunnel contraction has a 9:1 ratio, upstream of which the flow is conditioned by a honeycomb insert and a set of five wire-mesh screens, resulting in a free-stream turbulence intensity of less than 0.1% and an integral length scale of approximately $0.2c$, where c is the airfoil chord length. Furthermore, the free-stream velocity fluctuations were verified to have no significant spectral content within the frequency range of interest to this investigation, $100 \leq f \leq 2000$ Hz ($2 \leq St \leq 42$), where f denotes frequency and the Strouhal number is defined as $St = fc/U_0$. The test section free-stream velocity, U_0, was set based on the static pressure drop across the contraction calibrated against a Pitot-static tube in the empty test section, and was verified to be uniform within $\pm 0.5\%$ over 95% of the test section span.

All experiments were conducted using a NACA 0018 airfoil model with a chord length and span of 0.2 m and 0.61 m, respectively. An angle of attack of $4^\circ \pm 0.1$ was investigated at a free-stream velocity of $U_0 = 9.6\,\mathrm{m\,s^{-1}} \pm 0.2$, corresponding to a Reynolds number ($Re_c = U_0 c/\nu$) of approximately 125 000. The flow was forced by means of acoustic excitation, with a sub-woofer placed in the test section six chord lengths downstream from the airfoil. The presence of the sub-woofer in the test section was verified via mean surface pressure measurements to have no measurable impact on the mean characteristics of the flow. A 4189 Brüel and Kjær condenser microphone was used to characterize the acoustic environment, consisting of background noise and excitation at the airfoil surface. In addition to the unperturbed case, where the flow was left to develop naturally, two excitation cases were considered: (i) tonal excitation at the frequency of the most amplified disturbances in the unperturbed flow, i.e., the fundamental frequency (St_0), and (ii) tonal excitation at the subharmonic of the fundamental frequency ($\frac{1}{2}St_0$). In order to ensure proper comparison between the excitation cases, care was taken to ensure equivalent acoustic input levels within $2 \leq St \leq 42$. To this end, the sound pressure level (SPL) within this frequency range was

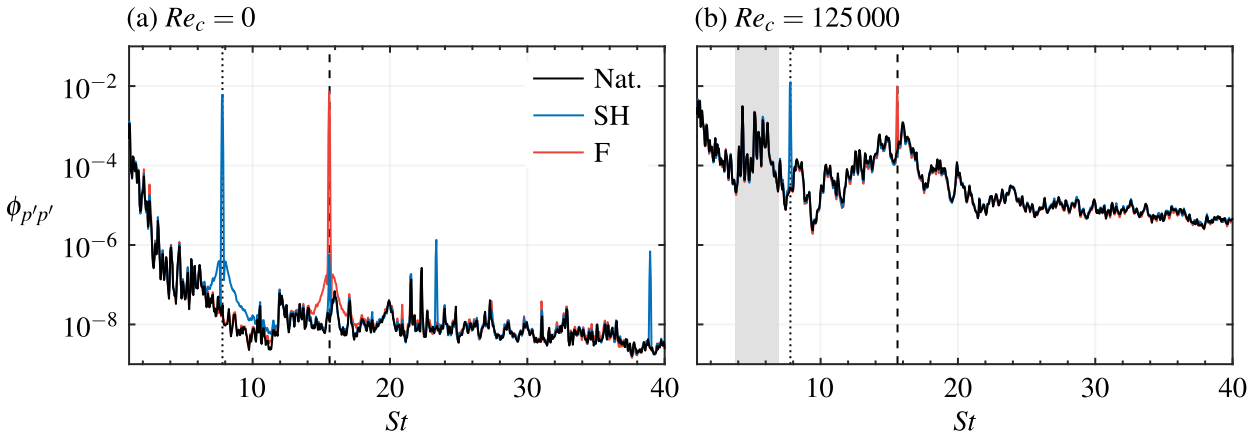

FIG. 1. Spectra of fluctuating pressure ($\phi_{p'p'}$) measured near the natural separation point for the natural (Nat.), fundamental (F) and subharmonic (SH) cases in (a) quiescent and (b) the investigated flow conditions. Dashed and dotted lines denote St_0 and $\frac{1}{2}St_0$, respectively. Gray shaded region indicates frequencies associated with test section standing wave.

kept at 89.5 dB for both the fundamental and subharmonic tone cases. In comparison, the SPL for the natural case was 87.1 dB.

Excitation levels at the airfoil surface were also characterized using an embedded microphone array [65], for which each individual microphone was calibrated against the reference Brüel and Kjær microphone used to characterize sound pressure levels in the test section. Spectra of the fluctuating pressure measured near the natural separation point are presented in Fig. 1. Figure 1(a) presents spectra corresponding to the two types of acoustic excitation which are compared to the spectrum of background pressure fluctuations in quiescent conditions. It can be seen that each excitation primarily produces elevated spectral content at the intended frequency and does not incite any resonant modes in the test facility. For the subharmonic case, peaks at higher harmonics are detectable, however, their amplitude are four orders of magnitude less than that at the targeted frequency. Spectra corresponding to the same location at $Re_c = 125\,000$ are presented in Fig. 1(b). In comparison to quiescent conditions, all spectra here show elevated energy content over a broad range of frequencies centered at St_0, which is attributed to transition occurring within the separation bubble. Furthermore, the spectra are devoid of significant spectral peaks at extraneous frequencies, therefore ensuring no unexpected narrow-band acoustic sources are influencing the transition process. However, relatively broadband acoustic activity is present around $St = 5$ [gray shaded region in Fig. 1(b)], which is due to acoustic standing waves that establish in all hard walled test sections [66–69]. The frequencies associated with this standing wave are denoted by St_{sw}, and their effect on flow development and transition is assessed in Sec. III.

Time-resolved, two-component PIV was employed in the two separate configurations to characterize the flow development in the separation bubble and the effect of forcing. The tests were performed in the configurations depicted in Fig. 2, where the surface attached coordinate system is indicated. Here, the x, y, and z coordinates correspond to the streamwise, wall-normal, and spanwise directions, respectively. The flow was seeded using a glycol-water-based fog with a mean particle diameter on the order of 1 µm, whose characteristic response frequency [70, 71] is above the Nyquist limit of the PIV sampling frequencies. The flow was illuminated by a laser sheet produced by a Photonics DM20-527 Nd:YLF pulsed laser, whose beam was conditioned into a sheet approximately 1 mm in thickness. For the side-view configuration [Fig. 2(a)], the sheet was

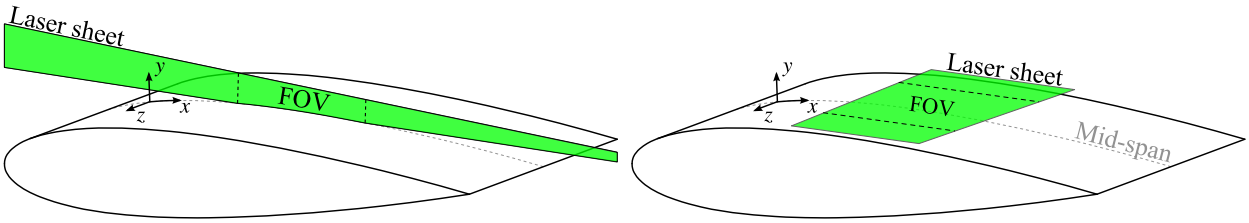

(a) Side-view (b) Top-view

FIG. 2. Experimental configurations for PIV measurements showing the surface-attached coordinate system, whose origin is located at the leading edge and midspan point.

positioned in the x-y plane. For the top-view [Fig. 2(b)], the sheet was oriented parallel to the local surface tangent at the center of the investigated field of view (FOV), where the center of the sheet was approximately 1.8 mm from the surface, with this distance increasing to 2.8 mm at the FOV edges. For both configurations, images were captured by two Photron SA4 high-speed cameras, which were synchronized with the laser via a timing unit controlled through LaVision's DaVis 8 software.

Table I provides an overview of the parameters for the PIV experiments. For the side-view PIV configuration [Fig. 2(a)], the cameras were fitted with Nikon 200 mm focal length macro lenses set to an aperture number ($f_\#$) of 4. The cameras' sensors were cropped to 1024×512 px and the fields of view were selected to maximize the spatial resolution in the aft portion of the separation bubble, while maintaining equal magnification factors of 0.67. The fields of view were overlapped by 10%, covering a total area of 54×12.5 mm, and double-frame images were acquired at 3.8 kHz. For the top-view PIV measurements [Fig. 2(b)], the cameras were fitted with 105 mm focal length macro lenses set to $f_\# = 2.8$. The streamwise extent of the FOV was set to match that of the combined side-view FOV, with the second camera employed to extend the FOV in the spanwise direction, while maintaining a 10% overlap. For both cameras, the full sensor resolution of 1024×1024 px and equal magnification factors of 0.33 were used. The combined top-view FOV is 54×102 mm, with double-frame images acquired at a rate of 1.9 kHz.

Image sampling and processing were performed in LaVision's DaVis 8 software. For both configurations, the focus was adjusted to produce imaged particles approximately 2 to 3 px in diameter. An iterative, multigrid cross-correlation scheme with window deformation [72] was used to compute velocity fields. A final interrogation window size of 16×16 pixels with 75% overlap was selected, with each window containing, on average, 14 particles. The resultant vector pitches in the PIV data are 0.12 and 0.24 mm for the side and top-view configurations, respectively. The results were post-processed using the universal outlier detection algorithm [73]. Individual velocity fields were then interpolated onto the common surface-attached coordinate system, with a cosine weighted blending function employed in the overlap region. The random errors in the PIV measurements were evaluated using the correlation statistics method [74]. The average uncertainties within the region of the separated shear layer are estimated to be less than 6% and 6.5% of U_0 for the side and top-view configurations, respectively, while higher uncertainties (approximately 10% of U_0) are present near the wall for the side-view configuration. Comparable uncertainties for the two configurations were achieved by minimizing the out-of-plane loss of particles for the top view by selecting a shorter frame separation time (Table I). Uncertainty estimates for all critical quantities derived from the PIV measurements are obtained through uncertainty propagation [75].

TABLE I. PIV parameters.

Parameter	Side view	Top view	Unit
Laser	Photonics DM20-527		
Cameras	Photron SA4		
Lens focal length	200	105	mm
Lens $f_\#$	4	2.8	
Magnification factor	0.67	0.33	
Sensor resolution	1024×512	1024×1024	px
Total field of view	54×12.5	54×102	mm
PIV mode	Double-frame		
Sampling rate	3.8	1.95	kHz
Frame separation time	40	60	µs
Outer flow displacement	17	9	px
Number of samples	5000	2728	
Window size	16×16		px
Vector pitch	0.12	0.24	mm

III. RESULTS

The results presented here pertain to a laminar separation bubble formed on the suction side of a NACA 0018 airfoil at an angle of attack of 4° and chord-based Reynolds number of 125 000. In addition to leaving the flow to develop naturally, tonal acoustic excitation is applied at the frequency of the most amplified disturbances in the natural flow, $St_0 = 15.6$ ($f_0 = 750\,\mathrm{Hz}$), and at the first subharmonic of St_0, $\frac{1}{2}St_0 = 7.8$ ($\frac{1}{2}f_0 = 375\,\mathrm{Hz}$), which were determined *a priori* via fluctuating surface pressure measurements (Fig. 1). Throughout the presentation of results, the natural, subharmonic and fundamental cases are denoted by Nat., SH, and F, respectively.

Time-averaged velocity field statistics are plotted in Fig. 3 and are analyzed to identify the presence and extent of the separation bubble. Displacement thickness is plotted alongside, $\delta^* = \int_0^\delta \left[1 - \frac{\overline{u}(y)}{U_\mathrm{e}}\right] \mathrm{d}y$, where δ and U_e are the local boundary layer thickness and edge velocity, respectively. A region of reverse flow is identifiable in the $\overline{u}$ contours of the natural flow, indicating the presence of flow separation and subsequent reattachment (in a time-averaged sense), and thus the formation of a separation bubble. The maximum reverse flow velocity is approximately 4% of U_0, thus indicating the flow is convectively unstable and is not subject to a global instability [16, 51, 76, 77]. The mean outline of the bubble is identified using the dividing streamline, which forms a closed contour with the surface within which the streamwise mass flux is zero [3, 4]. The intersection points of the dividing streamline with the surface are the mean separation (x_s) and reattachment (x_r) points, with the estimates of the former lying upstream of the measurement domain for all cases. The maximum bubble height and its streamwise position (x_h) are also indicated and are found where the maximum wall-normal distance between the surface and dividing streamline occurs. The uncertainties in determining x_s, x_h, and x_r are indicated by the dotted lines in Fig. 3, which are determined by propagating the PIV random errors estimates and the uncertainty in locating the airfoil surface through the determination of these locations.

From Fig. 3, neither type of excitation at the selected amplitude levels results in significant changes in the mean topology of the bubble, with all changes in mean separation, maximum

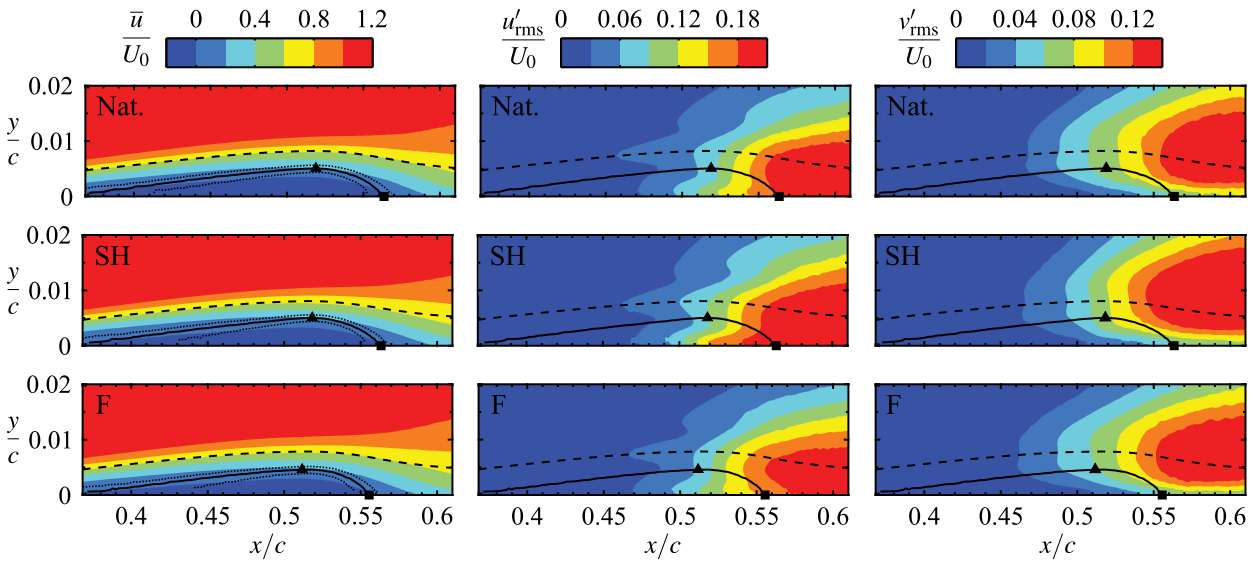

FIG. 3. Mean streamwise ($\overline{u}$), and rms of fluctuating (u'_{rms}, v'_{rms}) velocity contours. Solid lines mark the dividing streamlines, whose uncertainty limits are indicated by the dotted lines. Triangle and square markers denote mean maximum bubble height and reattachment points, respectively. Dashed lines indicate displacement thickness (δ^*).

bubble height, and reattachment falling within the experimental uncertainty. Accordingly, the root-mean-squares (rms) of streamwise (u'_{rms}) and wall-normal (v'_{rms}) velocity fluctuations are not appreciably altered by the excitation. Overall, the rms contours for all cases closely match previous reports for naturally developing separation bubbles [34, 36]. The rising rms levels along the trajectory of the displacement thickness indicate that the well-established process of streamwise disturbance amplification in the separated shear layer leading to roll up and the formation of shear layer vortices (e.g., Refs. 17 and 22) occurs in a similar manner for the cases presented in Fig. 3. However, subtle differences are detected in the rms contours, in particular in the near wall region of the u'_{rms} contours for the subharmonic case and in the v'_{rms} contours at $x/c = 0.46$ for both the subharmonic and fundamental cases, which indicates that flow development may be affected by the excitation.

A. Streamwise vortex development

Flow development within the separation bubble is assessed via the sequences of instantaneous spanwise vorticity contours presented in Fig. 4. Contours of the λ_2 criterion [78] are added to aid in identifying coherent structures. Animated sequences are provided as Supplementary Material [movies 1(a)–1(c)] [79]. The natural flow development [Fig. 4(a)] is characterized by periodic roll-up of the separated shear layer into vortices upstream of the maximum height location, $x_h/c = 0.52$. These structures interact and deform within $0.52 < x/c < 0.56$, followed by the onset of breakdown to smaller scales beyond mean reattachment, $x_r/c = 0.56$. Dashed lines are used to track the structure frame-to-frame, with the slope and streamwise spacing of the lines representing convective velocity and streamwise wavelength, respectively. The majority of structures in the naturally transitioning flow are characterized by similar convective velocities and wavelengths; however, sporadic merging between subsequent vortices can occur. This is captured for vortices

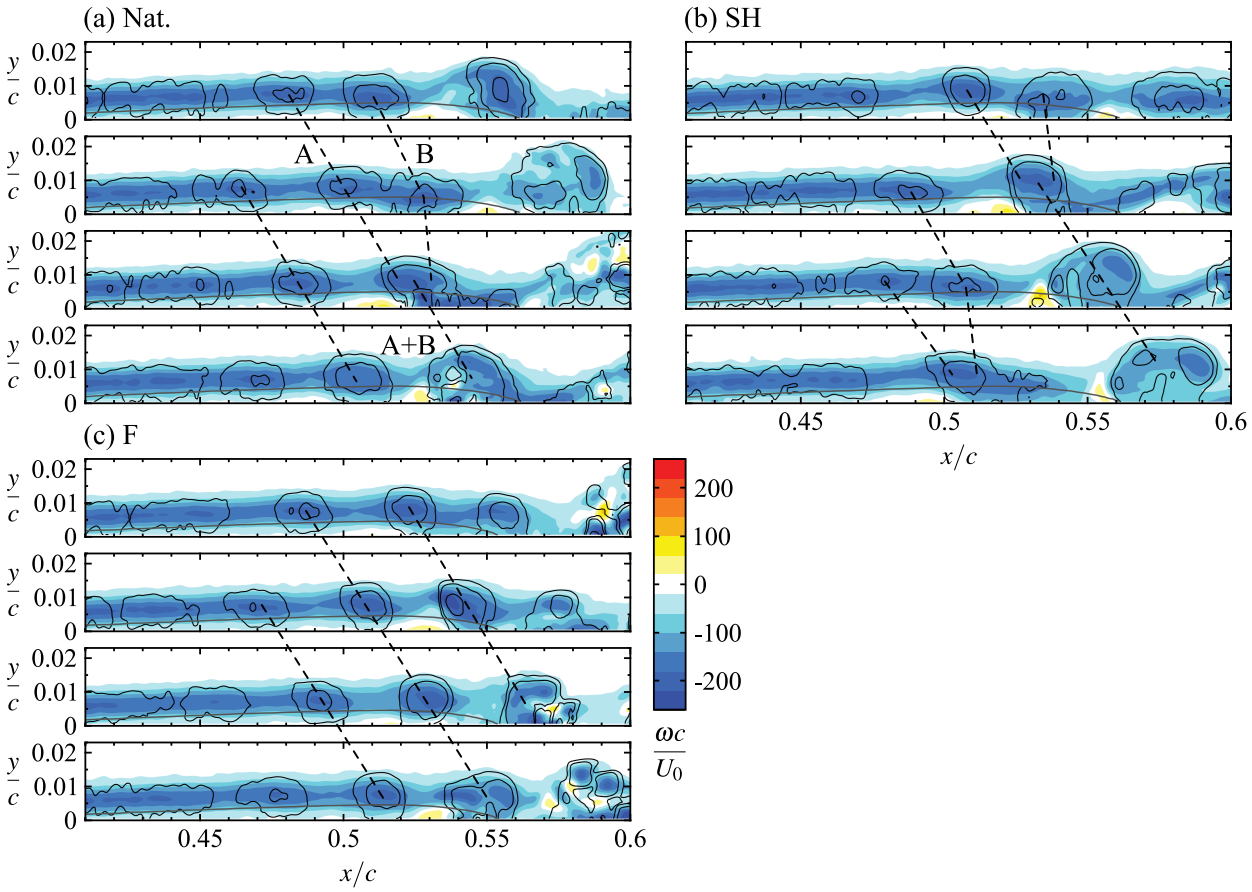

FIG. 4. Sequences of instantaneous spanwise vorticity (ω) contours. Consecutive frames are separated by $t^* = tU_0/c = 3.7 \times 10^{-2}$. Solid black lines indicate λ_2 contours [78]. Solid gray lines mark the dividing streamlines. Dashed lines trace the same vortices.

A and B in Fig. 4(a), where the convective velocity of the downstream structure in the merging pair (B) decreases, while that of the upstream vortex (A) remains constant. Consequently, the distance between the vortex cores decreases and they merge, forming A+B, which is separated from the nearest downstream vortex by approximately twice the average streamwise wavelength. The observed process is in general agreement with the stages of vortex merging described by Cerretelli and Williamson [48] and Meunier *et al.* [49].

Figures 4(b) and 4(c) show flow development in the LSB for the subharmonic and fundamental excited cases, respectively, where, similar to the natural case [Fig. 4(a)], the separated shear layer rolls up to form periodic vortices upstream of the maximum height location. The shed structures then convect downstream, deform, and eventually begin to break down to smaller scales. However, for the subharmonic case, vortex merging is observed regularly throughout the entire recorded sequence. This is exemplified by the results in Fig. 4(b), as all vortices initially identified in the roll-up region ($x/c < 0.53$) undergo merging. In stark contrast, Fig. 4(c) shows that forcing the flow at the fundamental frequency locks vortex shedding to the excitation frequency, evident from the significantly reduced variability in the convective velocity and streamwise wavelength of the shed structures. As such, vortex merging is difficult to identify through simple visual inspection and thus is speculated to be inhibited by the forcing applied at the fundamental frequency.

Wavelet analysis is employed to quantify the prevalence of vortex merging in the flow and the

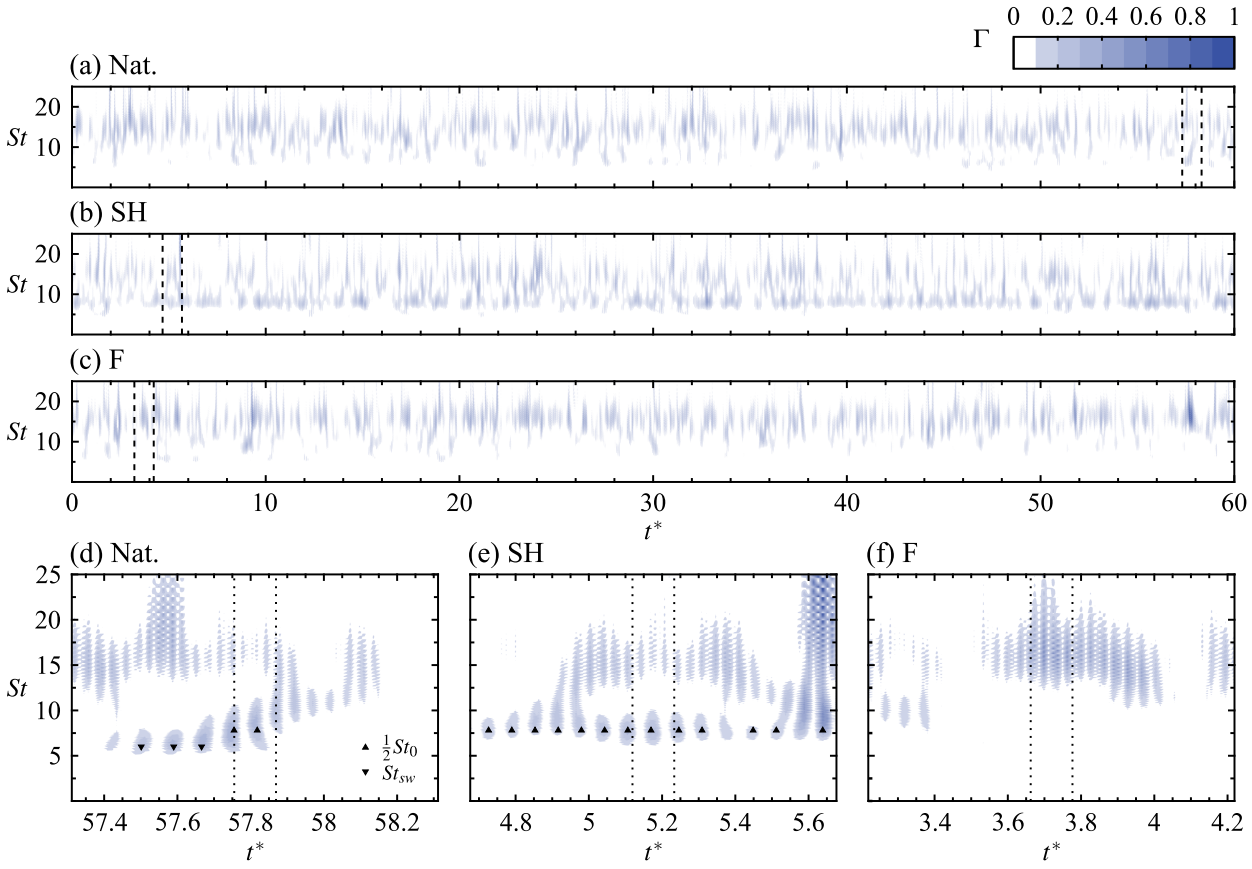

FIG. 5. Normalized wavelet coefficient (Γ) contours computed from wall-normal velocity fluctuations sampled at $y = \delta^*$ and the midpoint between x_h and x_r. Dashed regions in (a)–(c) replotted in (d)–(f). Dotted regions in (d)–(f) correspond to intervals shown in Fig. 4. Markers denote local maxima identified at frequencies of interest.

subsequent effect of forcing. This tool is preferred over traditional Fourier analysis since the merging phenomenon is localized in both time and space, while not necessarily being periodic in time. For each test case examined, fluctuating streamwise velocity time signals are extracted at $y = \delta^*$ and the midpoint between the mean maximum height and reattachment points ($x/c \approx 0.54$ for all cases), where most vortex merging events occur (Fig. 4). Wavelet coefficients are then calculated using the Morlet wavelet [80] for all time instants and across the relevant spectrum of frequencies, with the results presented in Fig. 5. For the natural and fundamental cases, examination of Figs. 5(a)–5(c) shows that velocity fluctuations are predominantly concentrated within a band of frequencies centered at $St_0 = 15.6$ over the entire recorded sequence. Instants at which significant wavelet coefficients exist at $\frac{1}{2}St_0 = 7.8$ do occur for these cases, however they are relatively infrequent compared to the subharmonic case, where activity at $\frac{1}{2}St_0$ is widespread over the entire measurement.

To link vortex merging with the trends observed in the wavelet coefficient contours, short segments that encompass the time periods corresponding to the vorticity sequences presented in Fig. 4 are shown in Figs. 5(d)–5(f). For the natural and subharmonic excited flows, when vortex merging is visually identified in Figs. 4(a) and 4(b), the corresponding maximum wavelet coefficients [within the dotted intervals in Fig. 5(d) and 5(e)] are concentrated at $\frac{1}{2}St_0$. In contrast, for the fundamental case [Fig. 5(c)], the wavelet coefficients are confined to a relatively narrow band cen-

tered at St_0, which is consistent with the highly organized and periodic nature of the structures observed in Fig. 4(c). Thus, the identification of local maxima in the wavelet coefficients at the frequencies of interest can serve to identify instances at which vortex merging occurs, allowing for a quantitative comparison of the prevalence of the phenomenon between the three studied cases. It must be noted that, in particular for the natural case [Fig. 5(d)], significant low-frequency activity is detected at $St_{sw} = 6$ in addition to $\frac{1}{2}St_0$. This activity is a result of the standing wave present in the test section [Fig. 1(b)], whose frequency is close to the subharmonic frequency. Therefore, it is possible that the standing wave serves to influence the flow, leading to merged structures with this characteristic frequency. For this reason, quantitative analysis for the results is performed for both $\frac{1}{2}St_0$ and St_{sw}, and the possible relation of the standing-wave frequency to vortex merging is considered in detail later in this section.

The proposed method for vortex merging quantification involves identifying all local maxima in the wavelet coefficients at the frequencies of interest, namely, $\frac{1}{2}St_0$ and St_{sw}, within a nondimensional frequency band of ± 0.1. Conditional filtering is applied, with a maximum only being retained if its magnitude exceeds a signal-to-noise ratio of five and is greater than other maxima detected at $St_0 \pm 0.1$ within a temporal window of width equal to twice the fundamental shedding period. The resulting detected maxima are indicated by the black markers in Figs. 5(d)–5(f). Estimates for the percentage of merged structures detected in the flow are made by taking the ratio of the combined number of maxima detected at $\frac{1}{2}St_0$ and St_{sw} to an estimated number of primary structures shed during the measurement sample (1.32 s) at the primary shedding frequency, $St_0 = 15.6$ ($f_0 = 750$ Hz). Prior to evaluating all data sets, the proposed methodology was applied to a test signal (0.35 s long) extracted at $y = \delta^*$ and the mid point between the mean maximum height and reattachment points from the subharmonic data set. Through a detailed manual inspection of the vorticity contours, it was determined that this test segment contained approximately 80 merging events, which the method was able to estimate within 4%. The method was then applied to the full data sets and at all streamwise positions, yielding the results shown in Fig. 6. The results are smoothed using a sliding spatial window ($0.01c$ width) and the indicated uncertainty bounds are determined based on the variability of estimates within the smoothing window. Note that results are plotted up until the mean reattachment locations, where the uncertainty was found to sharply increase from approximately $\pm 3\%$ to over $\pm 10\%$ due to the onset of vortex breakdown (Fig. 4).

Figure 6 provides several key insights regarding the vortex merging process and the effects of forcing. Namely, for all cases, no merged structures are detected in the fore portion of the bubble ($x/c > 0.48$), indicating that all vortices are formed and shed at the fundamental frequency. Further downstream, all cases show an eventual rise in the number of detected merged structures indicating the onset of merging, with the start of the region where R_{merg} plateaus indicating the location at which most merging events are completed. For the natural flow, the first merging events are detected at $x/c \approx 0.51$, followed by gradual increases in R_{merg} until it plateaus to a value of $9\% \pm 3$ at $x/c = 0.55$. Further downstream, R_{merg} begins to rise again, however, the changes are within the uncertainty of the estimates and may be a result of turbulent breakdown. For the subharmonic forcing, the onset of vortex merging is seen at a much earlier streamwise position compared to the natural flow, followed by a sharper rise in the ratio of merged structures that begins to plateau at $x/c = 0.53$, attaining a value of $34\% \pm 2$. Comparing the fundamental case to the natural flow, the ratio of detected merged structures also peaks at approximately $x/c = 0.55$, but the maximum value is reduced to $4\% \pm 1$. Thus, supporting the analysis of the time-resolved flow development (Fig. 4), these results conclusively show vortex merging occurs naturally in the studied LSB, while forcing at the subharmonic and fundamental frequencies promotes and

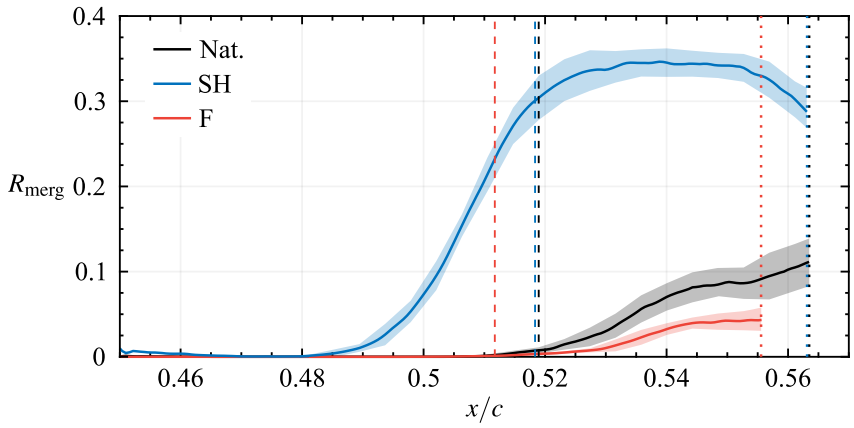

FIG. 6. Ratio of detected merged structures to total number of shed primary structures (R_{merg}) determined using wavelet methodology (cf. Fig. 5). Dashed and dotted lines (colored according to legend) mark x_h/c and x_r/c, respectively. Shaded regions (colored according to legend) indicate uncertainty bounds.

inhibits merging, respectively. Such observations are in agreement with those made for free shear layers [61, 62]. The results of this investigation clearly indicate that forcing specifically affects the streamwise position at which merging events take place and the total percentage of vortices that undergo merging.

From the peak ratio of detected merged structures determined from Fig. 6, it is possible to estimate the ratio of primary structures that are involved in vortex merging for a given case. For example, when the flow is forced subharmonically, at $x/c = 0.54$ the merged vortices account for 34% of the total number of shed primary vortices. Since merged structures are formed by two primary vortices, this implies that 68% of all primary vortices undergo merging. Similarly, the percentage of primary structures engaged in merging is 18% and 8% for the natural and fundamental forcing cases, respectively. In the investigation of Lambert and Yarusevych [38], they found that up to 15% of the total number of shed vortices merge in an unforced LSB formed over the same NACA 0018 profile at a comparable Reynolds number and angle of attack, which agrees well with the 18% reported here.

It is now possible to clarify the relationship between vortex merging and separation bubble topology given that the effects of forcing on vortex merging have been established. In free shear layers, it is well documented that the promotion of vortex merging through subharmonic forcing leads to an increase of momentum transfer across the layer [62]. For separation bubbles, it is generally accepted that mean reattachment is induced by the exchange of momentum from the outer flow to the wall by the shear layer vortices [33, 34]. Therefore, one might expect a promotion of vortex merging in an LSB to lead to earlier mean reattachment. However, the findings of this investigation clearly show this is not the case, as the percentage of primary structures that merge in the aft portion of the bubble increases significantly from 18% in the natural flow to 68% when forced subharmonically, yet the mean reattachment location does not change within the uncertainty of the PIV measurements (Fig. 3). This indicates that the enhancement of momentum exchange due to the increase in merged vortex circulation [48, 49] is balanced by the reduced frequency of the structures, producing a comparable mean flux of momentum to that produced by unmerged primary structures. Consequently, the mean bubble position, length, and maximum height remain largely unchanged (Fig. 3).

To quantify and compare the frequency content and streamwise growth of flow disturbances

across the studied cases, spectra of wall-normal velocity fluctuations in the separated shear layer (along $y = \delta^*$) are computed. The results are presented in Fig. 7, where one-dimensional frequency spectra are shown for increasing streamwise locations [Figs. 7(a)–7(c)], while two-dimensional, wave-number-frequency spectra are also presented [Figs. 7(d)–7(f)]. The former are computed by dividing signals into 2^{11} windows with 75% overlap, resulting in a nondimensional frequency resolution of 0.04, while for the latter, signals are divided into $2^{11} \times 2^9$ windows in time and x, respectively, with 75% overlap, resulting in St and streamwise wavenumber ($k_x c$) resolutions of 0.04 and 20, respectively. For the natural flow, Fig. 7(a) shows that disturbances within a band of frequencies centered on St_0 are first to be amplified and undergo convective amplification within $0.44 < x/c < 0.51$, i.e., upstream of the mean maximum height location. Beyond the maximum height location, the energy within the unstable frequency band is rapidly redistributed to a wide range of frequencies, consistent with the breakup of the rollers in the final stage of transition to turbulence observed in Fig. 4(a). Spectra for the subharmonic case, Fig. 7(b), show that the forcing does not alter the natural band of amplified disturbances appreciably; however, significant velocity fluctuations at $\frac{1}{2}St_0$ are detected at and beyond $x/c > 0.45$. The associated spectral energy is amplified within $0.45 < x/c < 0.51$, which maintains a relatively high amplitude beyond the mean reattachment location, despite the onset of the transition to turbulence. Overall, the observed trend in fluctuating energy content at $\frac{1}{2}St_0$ closely matches that of R_{merg} seen in Fig. 6, indicating the periodic passage of merged structures.

The spectra for the fundamental case [Fig. 7(c)] show strong disturbance growth at the excitation frequency, with no significant disturbance amplification at the subharmonic frequency, while some activity is observed in the spectra beginning at $x/c = 0.49$ and within $5 < St < 7$, which matches the frequency of the standing wave in the test section. In fact, this activity is present in the spectra for all three cases, and therefore indicates that the standing wave affects the flow development. In particular, for the natural and fundamental cases, the streamwise location at which amplification at St_{sw} begins is just upstream of where merged structures are first detected in Fig. 6, similar to growth at $\frac{1}{2}St_0$ in Fig. 7(b) preceding the detection of merged structures in Fig. 6 for the subharmonic case. Therefore these results support the earlier conjecture that the standing wave serves to influence the flow in a subharmonic fashion, leading to the formation of merged structures with this characteristic frequency. The link between the standing-wave frequency and vortex merging will be strengthened by the proper orthogonal decomposition (POD) analysis that follows in Sec. III B. That being said, an important distinction must be highlighted. Namely, vortex merging in the natural and fundamentally forced flows does not solely result due to the presence of the standing wave, but rather the process is influenced by the presence of the standing wave, resulting in merged structures with characteristics frequencies that match either the subharmonic or standing-wave frequencies, as seen in Fig. 5.

The wave-number-frequency spectra [Figs. 7(d)–7(f)] allow for determination of the predominant disturbance wavenumber and convective velocity. For all cases, spectral energy is primarily concentrated along a line of constant slope, which is commonly referred to as the convective ridge (e.g., Howe [81]). Along the convective ridge, the disturbance wavenumber and frequency are related by their convective velocity, $U_{\text{con}} = 2\pi f/k_x$. For the natural case [Fig. 7(d)], the wavenumber and convective velocity corresponding to St_0 are $k_x c = 150$ and $U_{\text{con}}/U_{\text{e}} = 0.55$, where U_{e} is the edge velocity taken outside of the separation bubble ($U_{\text{e}} = 1.2U_0$ from Fig. 3). The obtained estimate for U_{con} agrees well with the range $0.3 \lesssim U_{\text{con}}/U_{\text{e}} \lesssim 0.6$ observed in previous investigations [17, 26, 30, 60]. Figures 7(e) and 7(f) show that excitation at either the subharmonic or fundamental frequency concentrates spectral energy at the forcing frequency, while not appreciably altering the slope of the convective ridge. Estimating the convective velocities for these two

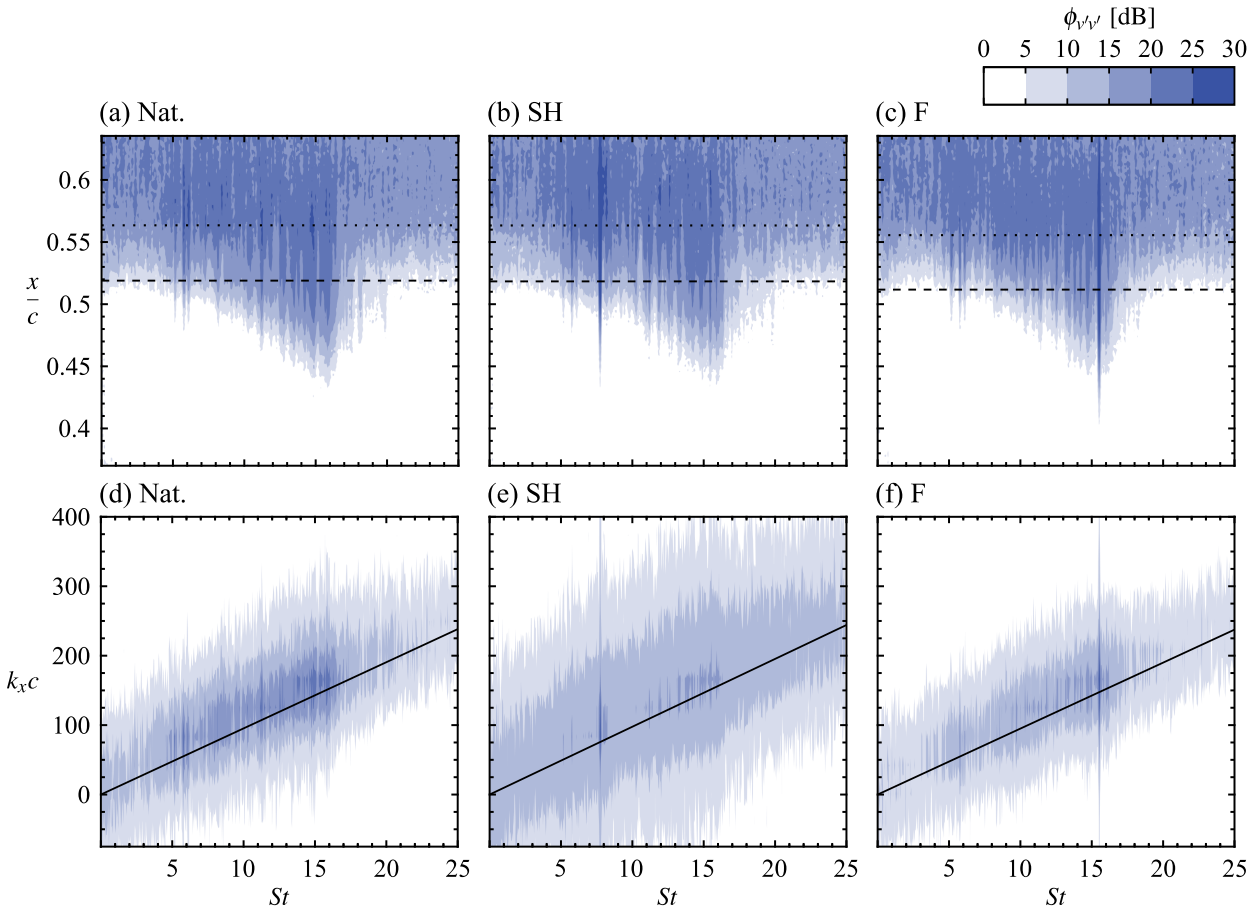

FIG. 7. Frequency [(a)–(c)] and wavenumber-frequency [(d)–(f)] spectra of wall-normal velocity fluctuations ($\phi_{v'v'}$) measured within the separated shear layer ($y = \delta^*$). Dashed and dotted lines mark x_h/c and x_r/c, respectively. Solid line is a linear fit estimating the convective ridge.

cases yields $U_{\mathrm{con}}/U_{\mathrm{e}} = 0.54$ and 0.55, respectively, which closely match that of the natural case. Therefore, consistent with ascertainable convective velocities from the vortex traces in Fig. 4, neither the promotion or suppression of vortex merging affects the convective velocity of the periodic disturbances.

The present results have established that, similar to free shear layers, targeted forcing applied at the subharmonic and fundamental frequencies promotes and inhibits vortex merging in an LSB, respectively. Further parallels can be drawn with free shear layers, as Ho and Huang [62] demonstrated that periodic vortex merging coincides with the growth of perturbation energy at the subharmonic frequency for acoustically forced free shear layers. A similar analysis is employed here, where modal amplitudes for perturbations of a given frequency are determined by integrating the frequency spectra within a nondimensional frequency band of width 1. The streamwise evolution of the computed amplitudes in the separated shear layer ($y = \delta^*$) is shown in Fig. 8, where St_0, $\frac{1}{2}St_0$, and St_{sw} are the frequencies of interest. When left to develop naturally [Fig. 8(a)], exponential growth is detected in the St_0 mode within $0.42 < x/c < 0.48$, followed by a reducing growth rate and eventual saturation by $x/c \approx 0.5$, which lies upstream of the mean maximum height location and coincides with the roll-up region, i.e., where coherent vortices are first formed. At the streamwise location where the fundamental mode begins to deviate from an exponential growth

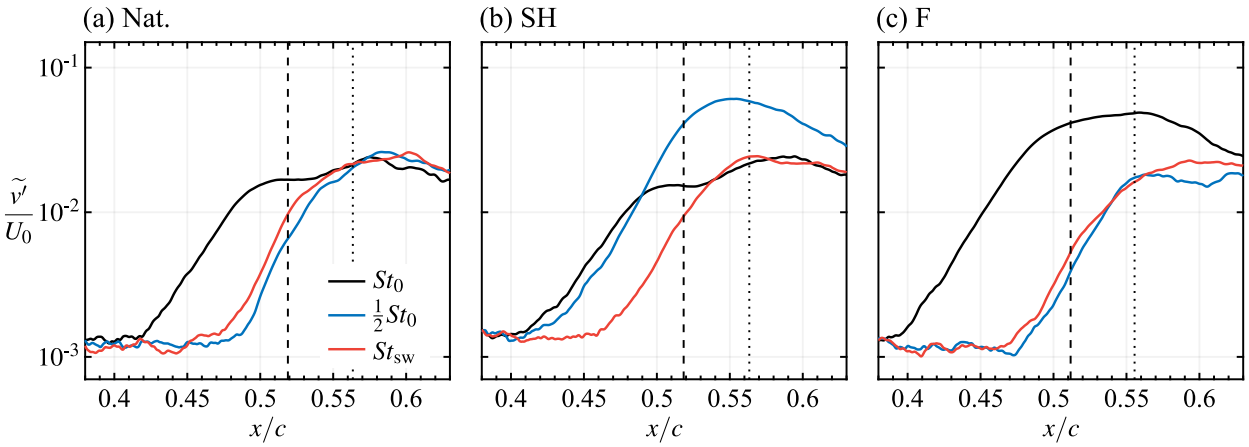

FIG. 8. Streamwise growth of frequency filtered wall-normal disturbances ($\widetilde{v'}$) within the separated shear layer ($y = \delta^*$). Dashed and dotted lines mark x_h/c and x_r/c, respectively.

rate ($x/c \approx 0.48$), growth is detected in the subharmonic and standing-wave modes, which precedes the detection of vortex merging onset as seen in Fig. 6. A similar progression is seen for the fundamental case [Fig. 8(c)], namely exponential growth in the fundamental mode followed by the growth in the other modes at a streamwise position slightly upstream of where vortex merging is first detected; however, here the earlier detectable growth in St_0 is observed as a result of forcing the fundamental mode.

In contrast to the natural and fundamental cases, when the flow is forced at the subharmonic frequency [Fig. 8(b)], both the St_0 and $\frac{1}{2}St_0$ modes undergo similar initial amplification. The fundamental mode then saturates at approximately the same streamwise location as that of the natural case, while the subharmonic mode continues to grow, reaching its peak at approximately $x/c = 0.55$. The streamwise location where this maximum is reached approximately coincides with where vortex merging is observed in Fig. 4(b) and where R_{merg} plateaus (Fig. 6), thus supporting the assertion of Ho and Huang [62]. In fact, the trends present in Fig. 8(b) agree well with those reported by Ho and Huang (see their Figs. 15 and 16). However, one distinction must be highlighted here, as a secondary harmonic resonance mechanism has been proposed for free shear layers [63, 64]. This mechanism dictates that the growth in the subharmonic mode follows the saturation of the fundamental mode, with subharmonic growth occurring as a result of energy cascading from the fundamental mode, even when forced at the subharmonic frequency. This appears not to be the case for the studied LSB, as here the subharmonic forcing is capable of affecting the intended mode directly without a secondary transfer mechanism.

B. Modal decomposition

To further analyze the effect of excitation on the coherent structure and their merging characteristics, Proper Orthogonal Decomposition is performed using the snapshot method of Sirovich [82]. Figure 9 presents the relative (E_r) and cumulative (E_c) energy distributions across the first 20 modes, with m denoting the mode number. As is typically seen for flows involving large-scale, propagating coherent structures [31, 34, 60, 83, 84], a significant portion of the total turbulent kinetic energy is captured within a small number of modes [$\sim$71%–78% in the first 20 modes, as seen in Fig. 9(b)], and the most energetic modes are grouped into pairs of similar energy levels

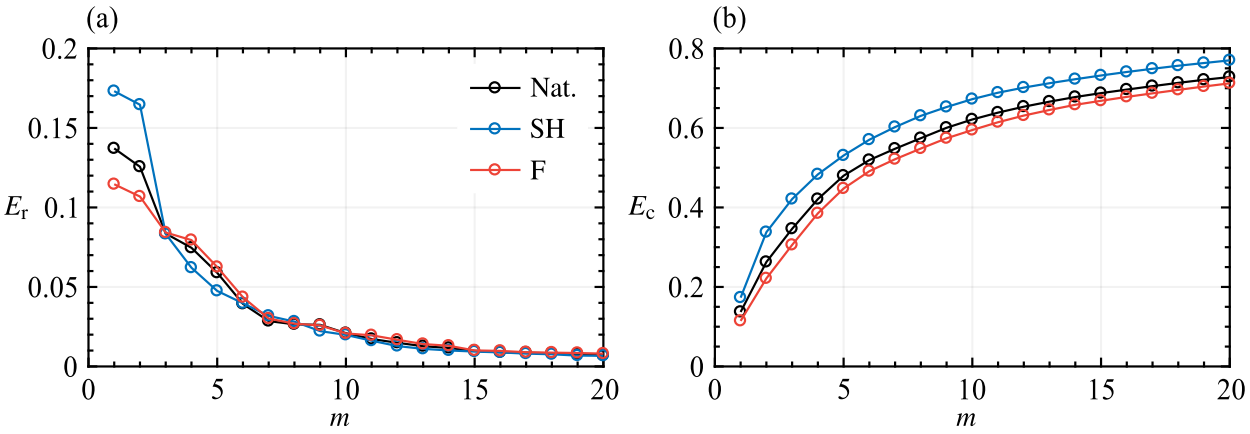

FIG. 9. POD (a) relative and (b) cumulative modal energy distributions.

[i.e., modes 1 and 2, and modes 3 and 4 in Fig. 9(a)]. The paired nature of the modes is confirmed through inspection of their spatial distribution, which show a distinct streamwise phase offset of $\pi/2$ between pairs. Therefore, every other mode is plotted in Fig. 10 for brevity. For all cases, the most energetic mode pair features a distinct periodic spatial structure that is characterized by a streamwise wavelength of approximately double the primary wavelength of the shear layer vortices in the natural flow [$\lambda_x/c \approx 0.04$ from Fig. 7(d)]. This, in addition to these structures being found in the aft portion of the bubble, indicates that these modes are associated with the merged shear layer vortices, while the unmerged, primary structures are captured by the higher mode pairs (modes 3 and 4 for the natural and fundamental cases, and modes 5 and 6 for all cases), as these structures have a wavelength of approximately $0.04c$ and form further upstream. Based on these results, several key observations can be made. First, the merged structures are the most energetic feature of the flow for all cases. Second, consistent with the effect of these two types of forcing on vortex merging, forcing at the subharmonic frequency increases the relative energy content of the modes associated with the merged structures, while the opposite effect is produced by the forcing applied at the fundamental frequency. It must be noted that a commensurate increase in the energy levels of the modes 3–6 is not seen when these modes are specifically targeted by forcing at the fundamental frequency [Fig. 9(a)], which has been previously reported [34]. This is likely a consequence of employing a spatial decomposition technique, resulting in modes with the same frequency content being split across several spatial modes. Thus, when the flow is forced small increases in the energy levels of many modes are observed, rather than a large increase for a single mode pair.

Further insight into the vortex merging process is gained through examination of the spectra of the POD temporal coefficients, presented in Fig. 11. Beginning with the subharmonic case [Fig. 11(b)], the results reveal that the most significant frequency content of the modes associated with the merged structures (e.g., $A^{(1)}$ and $A^{(3)}$) is found at $\frac{1}{2}St_0$, while the temporal coefficients for mode 5 show periodicity over a relatively broad range of frequencies centered at St_0. Thus, the previous analysis is confirmed in associating these modes with the merged and unmerged structures, respectively. For the natural and fundamental excitation cases [Figs. 11(a) and 11(c)], as expected, activity at St_0 is found for modes 3 and 5, while for mode 1 elevated energy levels are found at both $\frac{1}{2}St_0$ and St_{sw}. This further supports the previous assertion that the merged structures in the natural and fundamental excitation cases [$\Phi_v^{(1)}$ in Figs. 10(a) and 10(c)] are associated with a characteristic frequency that matches either the subharmonic or standing-wave frequencies.

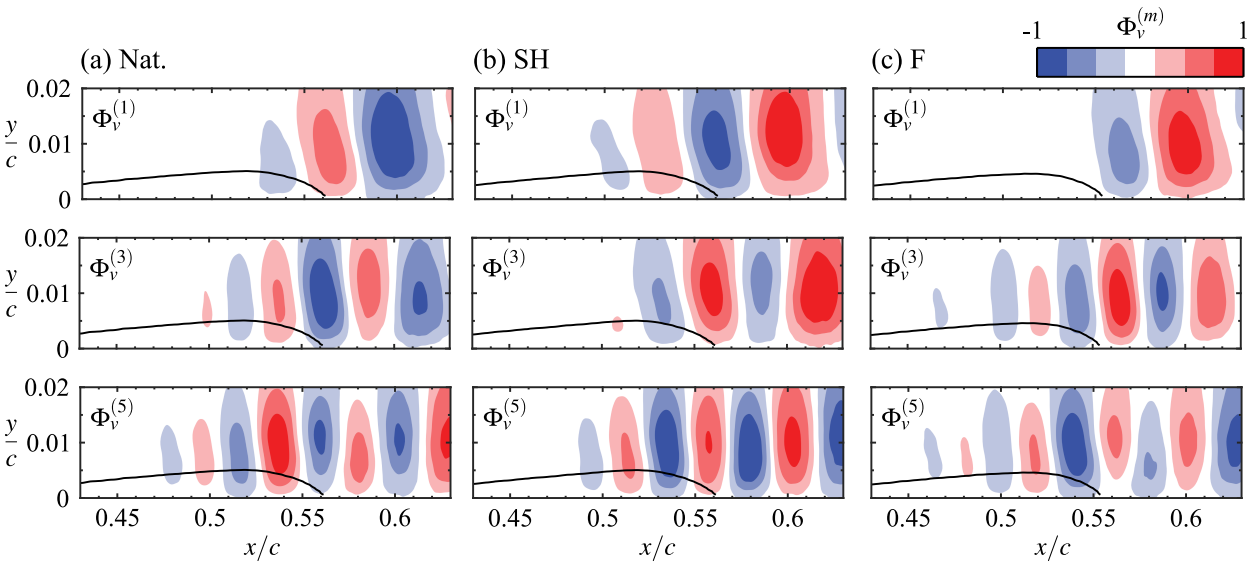

FIG. 10. Normalized POD spatial modes colored by the wall-normal component ($\Phi_v^{(m)}$). Solid lines mark the dividing streamlines.

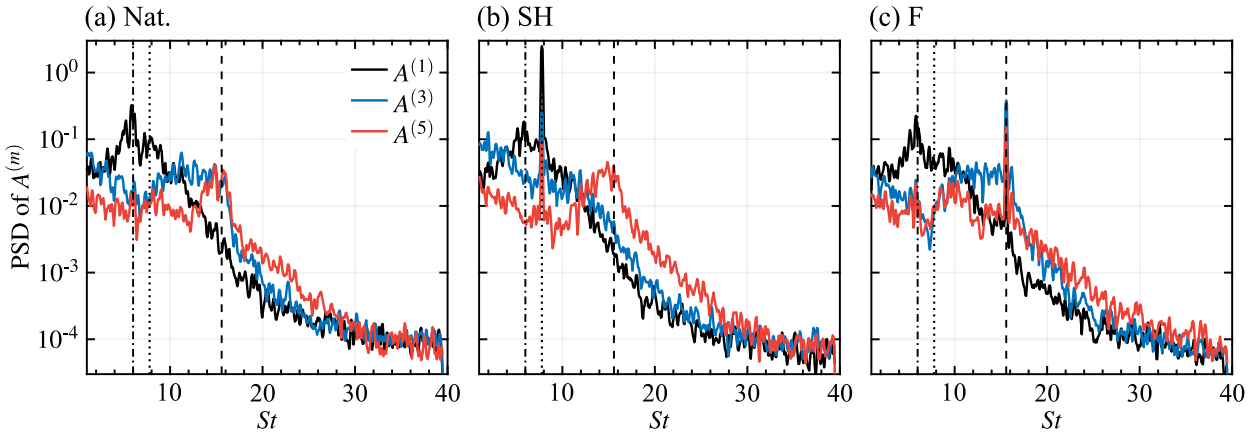

FIG. 11. Power spectral density (PSD) of POD temporal coefficients ($A^{(m)}$). Dashed, dotted, and dash-dotted lines mark St_0, $\frac{1}{2}St_0$, and St_{sw}, respectively.

To explore the contributions of the POD modes to the flow dynamics and the number of modes needed to accurately capture vortex shedding and merging, flow field reconstructions are performed using a truncated number of POD modes. Two exemplary cases are presented for the subharmonic excited flow in Figs. 12(a) and 12(b), showing reconstructions using the two and eight most energetic modes, respectively, which contain approximately 33% and 63% of the total turbulent kinetic energy, respectively. Animated sequences are provided as Supplementary Material (movies 2a and 2b) [79]. From Fig. 12(a), it is clear that the reconstruction based on the first two modes captures the merged structures, as the most upstream vortex is first identifiable in the aft portion of the bubble at a streamwise location that matches where the majority of merged structures are detected (Fig. 6) and where the subharmonic disturbance mode saturates [Fig. 8(b)]. Through iteration it has been verified that reconstructions using six to eight modes capture both the primary and merged structures. The reconstructed flow shown in Fig. 12(b) illustrates this, as

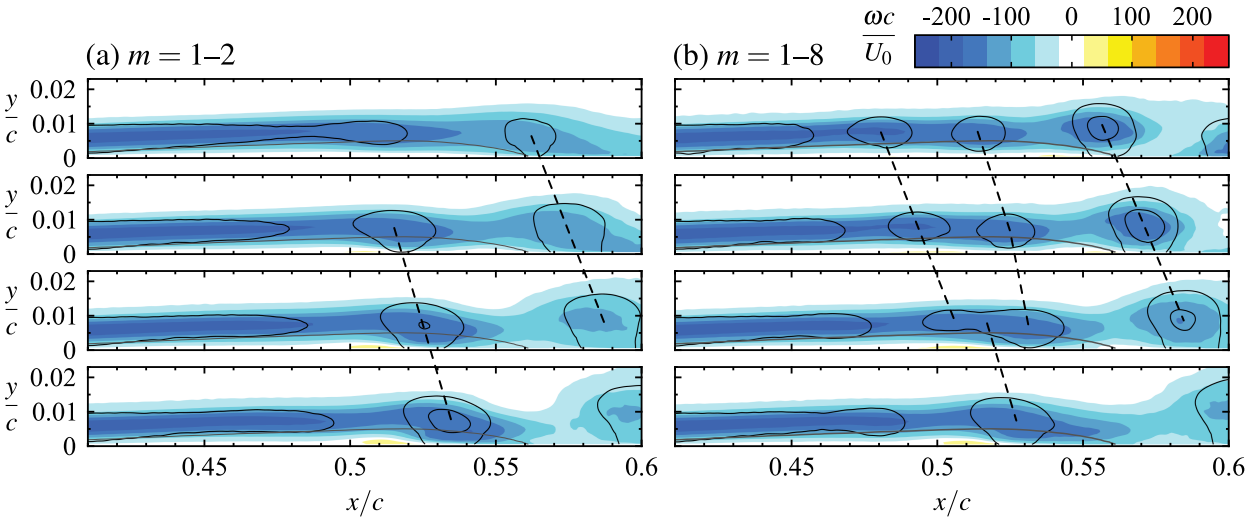

FIG. 12. Sequences of instantaneous spanwise vorticity contours constructed from POD reduced order models for the subharmonic excited flow. Models reconstructed used the (a) two and (b) eight most energetic modes. Consecutive frames are separated by $t^* = 2.5 \times 10^{-2}$. Solid black lines indicate λ_2 contours [78]. Solid gray lines mark the dividing streamlines. Dashed lines trace the same structures.

two primary vortices are shed upstream of the mean maximum bubble height location and merge with downstream development. It should be noted that this model only resolves the very basic dynamics of merging events [cf. Supplementary Material movie 2(b)] [79], which is improved by including more modes in the reconstruction.

C. Spanwise vortex development

The PIV measurements from the top view configuration [Fig. 2(b)] allow for analysis of both streamwise and spanwise aspects of the vortex merging process. For these measurements, the laser sheet was positioned such that it passed through the top halves of the roll-up vortices, thus allowing for their identification as periodic spanwise bands of high streamwise velocity in the planar images, which are visible throughout Fig. 13. For all cases, coherent and spanwise uniform structures are first identifiable at $x/c \approx 0.5$, which is consistent with where roll up is observed in Fig. 4. At and beyond formation, significant spanwise undulations develop in the vortex filaments, which intensify as the structures convect downstream. This leads to the onset of the breakup to smaller scales seen for $x/c > 0.6$.

For each of the studied cases, exemplary merging events are depicted in the sequences presented in Figs. 13(a)–13(c). Animated sequences are provided as Supplementary Material [movies 3(a)–3c] [79]. For example, Fig. 13(b) shows merging between two shear layer vortices, labeled as C and D, for the subharmonic excited flow. In Figs. 13(b-i) and 13(b-ii), vortex C convects downstream while developing spanwise undulations, which are most notable at $z/c = -0.1$ and 0.3, as the vortex filament bulges forward in the streamwise direction. Concurrently, vortex D is formed and also develops spanwise undulations in Figs. 13(b-ii) and 13(b-iii). The merging process between C and D begins to take place in Fig. 13(b-iii), as the vortex filaments intertwine, while the structures do not merge at the locations where the forward streamwise bulges developed in C. The merged structure, labeled as C+D in Fig. 13(b-iv), then continues to convect downstream

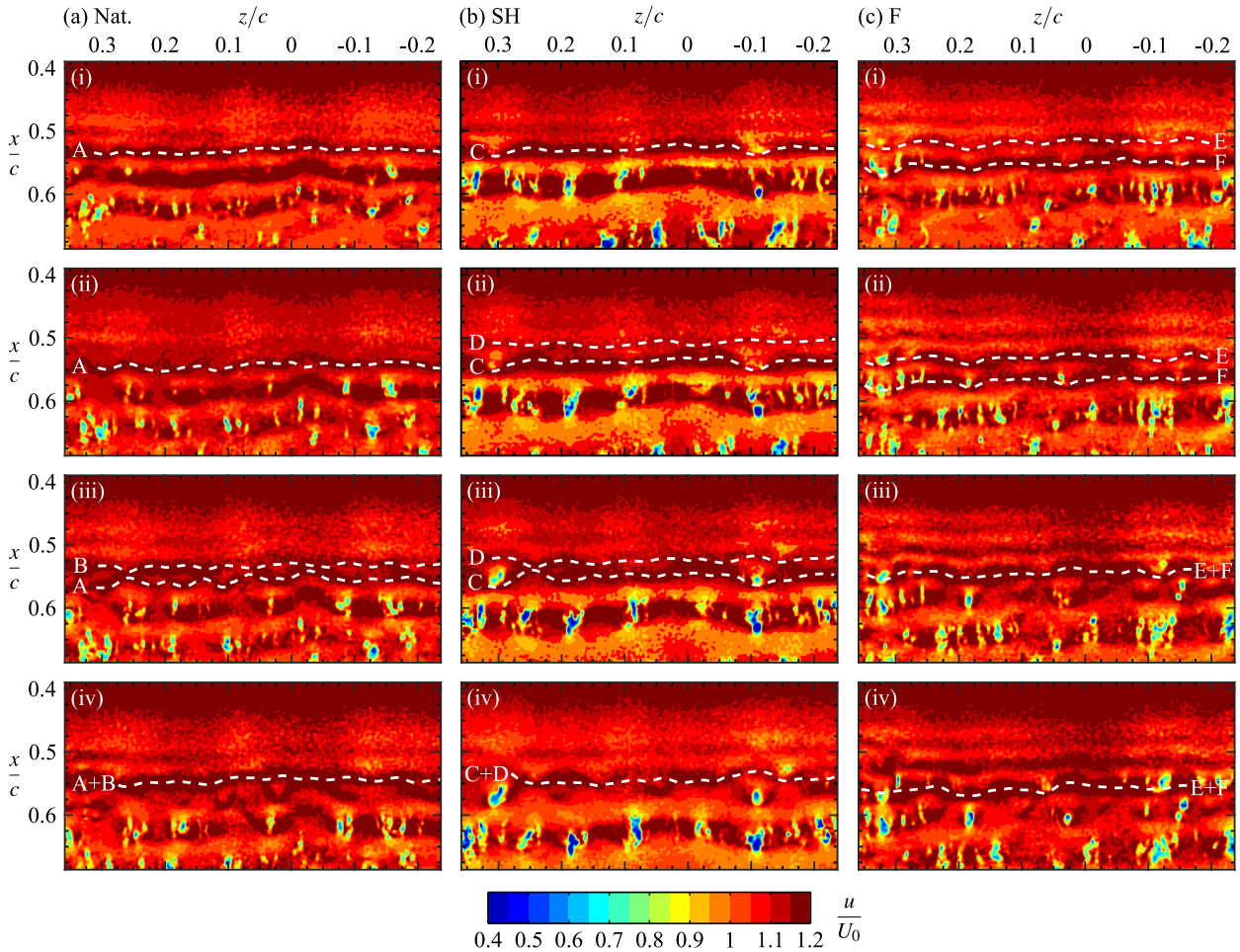

FIG. 13. Sequences of instantaneous streamwise velocity contours. Flow is from top to bottom. Consecutive frames are separated by $t^* = 2.5 \times 10^{-2}$. Dashed lines indicate smoothed spline fits to the center of selected structures (labeled A–F).

while retaining two separate vortex filaments over some spanwise segments, e.g., at $z/c \approx -0.1$ and 0.3. Overall, similar progressions are seen for the merging of structures A and B in the natural flow [Fig. 13(a)], and E and F in the flow excited at the fundamental frequency [Fig. 13(c)]. In particular, the depicted merging events occur in a nonuniform spanwise manner, resulting in structures that are merged within some spanwise segments, e.g., within $0.15 < z/c < 0.25$ and $0.05 < z/c < 0.15$ in Figs. 13(a-iv) and 13(c-iv), respectively, while distinct primary vortex filaments persist at other locations, e.g., at $z/c = 0.025$ and $z/c > 0.25$ in the same two figures. The three instances of vortex merging depicted here are representative of most merging events observed across the studied cases, and so the results demonstrate that vortex merging in a separation bubble occurs non-uniformly across the span, with the spanwise undulations that develop in the vortex filaments playing an intrinsic role in the process.

It should be noted that the spanwise wavelengths (λ_z) that develop in the vortex filaments exhibit significant cycle-to-cycle variations for all three cases. These variations were characterized in a statistical sense using a wavelet-based analysis described in Kurelek *et al.* [60]. Specifically, at each time instant, a wavelet transform is applied to streamwise velocity sampled along the $x/c = 0.55$ line to determine the dominant spanwise wavelength at that location at the given instant.

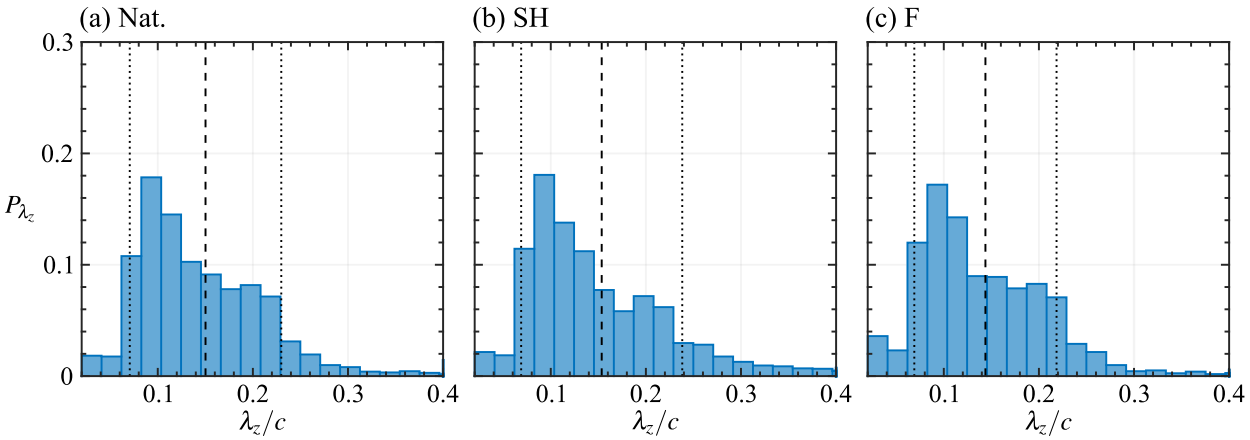

FIG. 14. Spanwise wavelength probability distributions (P_{λ_z}) at $x/c = 0.55$. Dotted lines indicate standard deviation from the mean (dashed line).

The resulting histograms are shown in Fig. 14, which show no appreciable differences across the three studied cases. Thus, it can be concluded that while the undulations that develop in the vortex filaments play an intrinsic role in the merging process, the effect of forcing on vortex merging does not manifest through modification of the spanwise wavelengths.

A statistical characterization of vortex merging was carried out using side-view PIV measurements taken at $z/c = 0$ [Fig. 2(a)], while results from the top-view measurements indicate that the process occurs in a spanwise nonuniform manner. Therefore, it is necessary to statistically characterize the spanwise behavior of vortex merging to evaluate if the results at $z/c = 0$ are representative of those over the full spanwise domain. This is carried out through an assessment of the spanwise variation in the ratio of detected merged structures over a range of streamwise locations using the previously employed wavelet methodology (cf. Fig. 5). The approach is unchanged from that previously described, save for the analysis is now applied to u' time signals from the top-view measurements. The signals are extracted across the span and at streamwise locations within $0.545 \leq x/c \leq 0.555$ for all cases. The results for each streamwise location are then averaged to give a single curve that is representative of the region where R_{merg} plateaus in Fig. 6. The results are presented in Fig. 15, which are smoothed using a sliding spatial window ($0.03c$ in width) and the indicated uncertainty bounds are determined based on the variability within the smoothing window. Evaluating R_{merg} at $z/c = 0$ for the natural, subharmonic and fundamental cases gives $7.5\% \pm 2$, $30\% \pm 4$, and $3.5\% \pm 3$, respectively, all of which are in good agreement with the values determined from the side-view analysis (9%, 34%, and 4%).

It should be noted that in applying the wavelet detection method to the top-view data, no attempt is made to correlate merging at a given spanwise location with other events occurring at the same instant in time. Thus, the results in Fig. 15 do not give any indication toward the spanwise uniformity of any given merging event, but rather give a measure of the overall variability in the prevalence of merging over the entire span, while also revealing statistical tendencies for merging events toward particular spanwise locations. Beginning with the natural case, the ratio of detected merged structures varies within $6.5\% \leq R_{\text{merg}} \leq 14.5\%$ over the spanwise extent of the measurement domain. Discernible peaks in R_{merg} can be identified, e.g., at $z/c = -0.16$, 0.15, and 0.25; however, the peak values fall well within the uncertainty bounds. The prevalence of merging events toward particular spanwise locations becomes clearer for the two forcing cases, where peaks in R_{merg} are found, some at the same spanwise locations (e.g., $z/c = -0.16$, 0.15, and

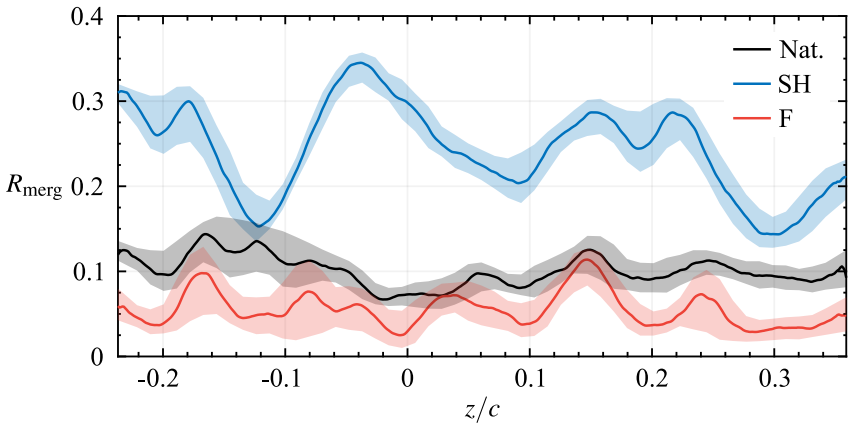

FIG. 15. Spanwise variation in ratio of detected merged structures to total number of shed primary structures using wavelet methodology (cf. Fig. 5). Method is evaluated at streamwise locations within $0.545 \leq x/c \leq 0.555$, with results averaged to produce a single curve representative of the region where R_{merg} plateaus in Fig. 6. Shaded regions (colored according to legend) indicate uncertainty bounds.

0.25). The most pronounced variability is observed for the case of subharmonic excitation, where the locations of the most prominent valleys in Fig. 15 (e.g., $z/c = -0.12$ and 0.3) correspond to locations in Fig. 13(b) where merging between vortices C and D is delayed. This indicates that local vortex merging tends to occur more often in certain flow regions, where in other regions merging is more likely to be delayed and may not complete before the onset of turbulent breakdown. In this experiment, careful attention was paid to the model and facility to prevent any spanwise modulation of the flow, and the fact that the number and location of the peaks and valleys in Fig. 15 differ across the cases suggests that the observed spanwise non-uniformity in the merging process is likely linked to LSB dynamics. Nevertheless, across the studied cases, it is apparent that there is significant variability in the prevalence of vortex merging across the span, with the ratio of detected merged structures varying by as much as 50% of the midspan value.

IV. CONCLUSIONS

The present investigation examined vortex merging in a laminar separation bubble. The bubble was formed on the suction side of a NACA 0018 airfoil in a closed-loop wind tunnel facility at a Reynolds number of 125 000 and an angle of attack of 4°. The vortex merging process in the bubble was manipulated through acoustic forcing applied as a tone at either the fundamental or subharmonic frequency of the most amplified instability in the natural flow. An objective comparison between all cases was made possible by keeping the forcing amplitude relatively low, with a constant sound pressure level increase of 2 dB above the natural level employed for both forcing cases. The flow field was assessed via time-resolved, two-component PIV. Two separate configurations were employed to evaluate streamwise and spanwise aspects of the flow development.

The results show that vortex merging occurs naturally in the separation bubble, while forcing at the subharmonic and fundamental frequencies promotes and inhibits merging, respectively. This was quantified through a merged vortex detection method, which was implemented based on wavelet analysis and was successful in identifying individual merging events. In applying the method to the studied cases, it was found that at the midspan 18% of primary structures formed in the naturally developing bubble merge, which increases to 64% when forced at the subharmonic

frequency and decreases to 8% when forced at the fundamental frequency. Furthermore, for all cases, the majority of merging events were found to occur in the aft portion of the bubble, i.e., downstream from the mean maximum bubble height location and upstream of mean reattachment, while subharmonic forcing leads to a significant number of merging events shifting upstream of the maximum bubble height location. Despite subharmonic forcing having a significant effect on the prevalence of vortex merging, the mean topology of the bubble is shown to remain relatively unchanged from the natural case. Since it is generally accepted that reattachment is facilitated by the vortices formed in a separation bubble [33, 34], these results imply that the increase in strength of individual structures as a result of merging is balanced by the reduction in frequency of the structures, resulting in a largely unchanged mean bubble topology.

In addition to merged structures with a characteristic frequency matching the subharmonic frequency, some merging events are found to be associated with a distinctly lower frequency. This activity is shown to be the result of the acoustic standing wave that establishes in the tunnel test section, whose contribution to the background disturbance spectrum results in merged structures with a characteristic frequency that matches either the subharmonic or standing-wave frequencies. POD analysis confirms this association, in addition to revealing that the merged structures are the most energetic flow features for all cases. Approximately 60%–70% of the total turbulent kinetic energy is found to be contained within the first six to eight POD modes, and so suitability toward low-order modeling is demonstrated as reconstructions using these modes are shown to be effective in capturing the basic vortex shedding and merging phenomena.

The results of this investigation are contrasted with those previously reported for free shear layer in order to highlight key similarities and differences between these canonical flows. In particular, through tracking the streamwise growth of modal amplitudes of velocity disturbances, it is demonstrated that the modes associated with vortex merging begin to grow just upstream of where vortex merging is first detected and saturate at the streamwise position at which the majority of merging events are completed. Such findings agree well with that observed in free shear layers [25, 62]; however, contrary to the proposed secondary harmonic resonance mechanism for free shear layers, here it is demonstrated that subharmonic forcing leads to concurrent growth in the fundamental and subharmonic modes. This indicates that subharmonic forcing in an LSB is capable of affecting the intended mode directly without a secondary transfer mechanism.

Examination of the spanwise behavior of the vortex merging process reveals that structures merge in a spanwise nonuniform manner, with localized merging occurring away from where forward and rearward streamwise bulges develop in the vortex filaments. Thus, the spanwise undulations that develop in the vortex filaments are shown to play an intrinsic role in LSB vortex merging. Through application of the merged vortex detection method to the spanwise measurements, the spanwise variability in the number of structures that merge is characterized. For the subharmonic forced case in particular, a preference for merging events at specific spanwise locations is demonstrated, with the number of primary structures that merge varying by as much as 50% between spanwise locations. Although variability is observed between the studied cases, for a given LSB, the undulations in the vortex filaments tend to develop in a consistent spanwise manner, leading to specific spanwise segments where merging tends to occur more frequently.

ACKNOWLEDGEMENTS

The authors gratefully acknowledge the Natural Sciences and Engineering Research Council of Canada (NSERC) for funding this work.

---

[1] I. Tani, "Low-speed flows involving bubble separations," Prog. Aerosp. Sci. **5**, 70–103 (1964).

[2] M. Gaster, "The Structure and Behaviour of Laminar Separation Bubbles," Aeronaut. Res. Counc. **RM 3595** (1967).

[3] H. P. Horton, *Laminar separation bubbles in two and three dimensional incompressible flow*, Ph.D. thesis, Queen Mary College, University of London (1968).

[4] M. O'Meara and Thomas J. Mueller, "Laminar separation bubble characteristics on an airfoil at low Reynolds numbers," AIAA J. **25**, 1033–1041 (1987).

[5] M. S. H. Boutilier and S. Yarusevych, "Parametric study of separation and transition characteristics over an airfoil at low Reynolds numbers," Exp. Fluids **52**, 1491–1506 (2012).

[6] T. J. Mueller and J. D. DeLaurier, "Aerodynamics of Small Vehicles," Annu. Rev. Fluid Mech. **35**, 89–111 (2003).

[7] H. P. Hodson and R. J. Howell, "The role of transition in high-lift low-pressure turbines for aero-engines," Prog. Aerosp. Sci. **41**, 419–454 (2005).

[8] B. H. Carmichael, *Low Reynolds Number Airfoil Survey*, Tech. Rep. (NASA Contract Report No. 165803, 1981).

[9] E. J. G. Arcondoulis, C. J. Doolan, A. C. Zander, and L. A. Brooks, "A review of trailing edge noise generated by airfoils at low to moderate Reynolds number," Acoust. Aust. **38**, 129–133 (2010).

[10] A. V. Boiko, G. R. Grek, A. V. Dovgal, and V. V. Kozlov, *The Origin of Turbulence in Near-Wall Flows* (Springer, 2002).

[11] C. P. Häggmark, A. A. Bakchinov, and P. H. Alfredsson, "Experiments on a two-dimensional laminar separation bubble," Philos. Trans. R. Soc. A Math. Phys. Eng. Sci. **358**, 3193–3205 (2000).

[12] O. Marxen, M. Lang, U. Rist, and S. Wagner, "A Combined Experimental/Numerical Study of Unsteady Phenomena in a Laminar Separation Bubble," Flow, Turbul. Combust. **71**, 133–146 (2003).

[13] S. K. Roberts and M. I. Yaras, "Large-Eddy Simulation of Transition in a Separation Bubble," J. Fluids Eng. **128**, 232 (2006).

[14] S. S. Diwan and O. N. Ramesh, "On the origin of the inflectional instability of a laminar separation bubble," J. Fluid Mech. **629**, 263–298 (2009).

[15] C. P. Häggmark, C. Hildings, and D. S. Henningson, "A numerical and experimental study of a transitional separation bubble," Aerosp. Sci. Technol. **5**, 317–328 (2001).

[16] U. Rist and U. Maucher, "Investigations of time-growing instabilities in laminar separation bubbles," Eur. J. Mech. - B/Fluids **21**, 495–509 (2002).

[17] M. S. H. Boutilier and S. Yarusevych, "Separated shear layer transition over an airfoil at a low Reynolds number," Phys. Fluids **24**, 084105 (2012).

[18] O. Marxen and U. Rist, "Mean flow deformation in a laminar separation bubble: separation and stability characteristics," J. Fluid Mech. **660**, 37–54 (2010).

[19] O. Marxen, M. Lang, and U. Rist, "Discrete linear local eigenmodes in a separating laminar boundary layer," J. Fluid Mech. **711**, 1–26 (2012).

[20] O. Marxen, R. B. Kotapati, R. Mittal, and T. Zaki, "Stability analysis of separated flows subject to control by zero-net-mass-flux jet," Phys. Fluids **27**, 024107 (2015).

[21] S. Yarusevych and M. Kotsonis, "Steady and transient response of a laminar separation bubble to controlled disturbances," J. Fluid Mech. **813**, 955–990 (2017).

[22] J. H. Watmuff, "Evolution of a wave packet into vortex loops in a laminar separation bubble," J. Fluid Mech. **31**, 119–169 (1999).

[23] T. Herbert, "Secondary Instability Of Boundary Layers," Annu. Rev. Fluid Mech. **20**, 487–526 (1988).

[24] C. H. K. Williamson, "Vortex Dynamics in the Cylinder Wake," Annu. Rev. Fluid Mech. **28**, 477–539 (1996).

[25] C.-M. Ho and P. Huerre, "Perturbed Free Shear Layers," Annu. Rev. Fluid Mech. **16**, 365–424 (1984).

[26] S. Burgmann and W. Schröder, "Investigation of the vortex induced unsteadiness of a separation bubble via time-resolved and scanning PIV measurements," Exp. Fluids **45**, 675–691 (2008).

[27] L. E. Jones, R.D. Sandberg, and N. D. Sandham, "Direct numerical simulations of forced and unforced separation bubbles on an airfoil at incidence," J. Fluid Mech. **602**, 175–207 (2008).

[28] S. Yarusevych, P. E. Sullivan, and J. G. Kawall, "On vortex shedding from an airfoil in low-Reynolds-number flows," J. Fluid Mech. **632**, 245–271 (2009).

[29] O. Marxen, M. Lang, and U. Rist, "Vortex Formation and Vortex Breakup in a Laminar Separation Bubble," J. Fluid Mech. **728**, 58–90 (2013).

[30] S. Pröbsting and S. Yarusevych, "Laminar separation bubble development on an airfoil emitting tonal noise," J. Fluid Mech. **780**, 167–191 (2015).

[31] D. Lengani, D. Simoni, M. Ubaldi, and P. Zunino, "POD analysis of the unsteady behavior of a laminar separation bubble," Exp. Therm. Fluid Sci. **58**, 70–79 (2014).

[32] D. Lengani, D. Simoni, M. Ubaldi, P. Zunino, and F. Bertini, "Analysis of the Reynolds stress component production in a laminar separation bubble," Int. J. Heat Fluid Flow **64**, 112–119 (2017).

[33] O. Marxen and D. S. Henningson, "The effect of small-amplitude convective disturbances on the size and bursting of a laminar separation bubble," J. Fluid Mech. **671**, 1–33 (2011).

[34] S. Yarusevych and M. Kotsonis, "Effect of Local DBD Plasma Actuation on Transition in a Laminar Separation Bubble," Flow, Turbul. Combust. **98**, 195–216 (2017).

[35] A. Nati, R. de Kat, F. Scarano, and B. W. van Oudheusden, "Dynamic pitching effect on a laminar separation bubble," Exp. Fluids **56**, 172 (2015).

[36] J. W. Kurelek, A. R. Lambert, and S. Yarusevych, "Coherent Structures in the Transition Process of a Laminar Separation Bubble," AIAA J. **54**, 2295–2309 (2016).

[37] T. M. Kirk and S. Yarusevych, "Vortex shedding within laminar separation bubbles forming over an airfoil," Exp. Fluids **58**, 43 (2017).

[38] A. R. Lambert and S. Yarusevych, "Characterization of Vortex Dynamics in a Laminar Separation Bubble," AIAA J. **55**, 2664–2675 (2017).

[39] R. Hain, C. J. Kähler, and R. Radespiel, "Dynamics of laminar separation bubbles at low-Reynolds-number aerofoils," J. Fluid Mech. **630**, 129–153 (2009).

[40] E. Wolf, C. J. Kähler, D. R. Troolin, C. Kykal, and W. Lai, "Time-resolved volumetric particle tracking velocimetry of large-scale vortex structures from the reattachment region of a laminar separation bubble to the wake," Exp. Fluids **50**, 977–988 (2011).

[41] T. Michelis, S. Yarusevych, and M. Kotsonis, "On the origin of spanwise vortex deformations in laminar separation bubbles," J. Fluid Mech. **841**, 81–108 (2018).

[42] J. C. McWilliams, "The vortices of two-dimensional turbulence," J. Fluid Mech. **219**, 361–385 (1990).

[43] A. Vincent and M. Meneguzzi, "The satial structure and statistical properties of homogeneous turbulence," J. Fluid Mech. **225**, 1–20 (1991).

[44] J. Jiménez, H. K. Moffatt, and C. Vasco, "The structure of the vortices in freely decaying two-dimensional turbulence," J. Fluid Mech. **313**, 209–222 (1996).

[45] H. J. H. Clercx, S. R. Maassen, and G. J. F. van Heijst, "Decaying two-dimensional turbulence in square containers with no-slip or stress-free boundaries," Phys. Fluids **11**, 1963–1963 (1999).

[46] P. Huerre and M. Rossi, "Hydrodynamic instabilities in open flows," in *Hydrodyn. Nonlinear Instab.*, edited by C. Godreche and P. Manneville (Cambridge University Press, 1998).

[47] E. J. Hopfinger and G. J. F. van Heijst, "Vortices in Rotating Fluids," Annu. Rev. Fluid Mech. **25**, 241–289 (1993).

[48] C. Cerretelli and C. Williamson, "The physical mechanism for vortex merging," J. Fluid Mech. **475**, 41–77 (2003).

[49] P. Meunier, S. Le Dizès, and T. Leweke, "Physics of vortex merging," Comptes Rendus Phys. **6**, 431–450 (2005).

[50] V. Kibens, "Discrete Noise Spectrum Generated by Acoustically Excited Jet," AIAA J. **18**, 434–441 (1980).

[51] M. Alam and N. D. Sandham, "Direct numerical simulation of 'short' laminar separation bubbles with turbulent reattachment," J. Fluid Mech. **403**, 223–250 (2000).

[52] U. Rist, M. Lang, and S. Wagner, "Investigations on controlled transition development in a laminar separation bubble by means of LDA and PIV," Exp. Fluids **36**, 43–52 (2004).

[53] L. E. Jones, R. D. Sandberg, and N. D. Sandham, "Stability and Receptivity Characteristics of a Laminar Separation Bubble on an Aerofoil," J. Fluid Mech. **648**, 257–296 (2010).

[54] M. Amitay and A. Glezer, "Role of Actuation Frequency in Controlled Flow Reattachment over a Stalled Airfoil," AIAA J. **40**, 209–216 (2002).

[55] A. Glezer, M Amitay, and A. M. Honohan, "Aspects of Low- and High-Frequency Actuation for Aerodynamic Flow Control," AIAA J. **43**, 1501–1511 (2005).

[56] K. B. M. Q. Zaman, A. Bar-Sever, and S. M. Mangalam, "Effect of acoustic excitation on the flow over a low- Re airfoil," J. Fluid Mech. **182**, 127–148 (1987).

[57] M. Nishioka, M. Asai, and S. Yoshida, "Control of flow separation by acoustic excitation," AIAA J. **28**, 1909–1915 (1990).

[58] S. Yarusevych, P. E. Sullivan, and J. G. Kawall, "Effect of Acoustic Excitation Amplitude on Airfoil Boundary Layer and Wake Development," AIAA J. **45**, 760–771 (2007).

[59] S. Yarusevych, J. G. Kawall, and P. E. Sullivan, "Airfoil Performance at Low Reynolds Numbers in the Presence of Periodic Disturbances," J. Fluids Eng. **128**, 587 (2006).

[60] J. W. Kurelek, M. Kotsonis, and S. Yarusevych, "Transition in a separation bubble under tonal and broadband acoustic excitation," J. Fluid Mech. **853**, 1–36 (2018).

[61] P. Huerre, "Open Shear Flow Instabilities," in *Perspect. Fluid Dyn. A Collect. Introd. to Curr. Res.*, edited by G. K. Batchelor, H. K. Moffatt, and M. G. Worster (Cambridge University Press, 2000) pp. 159–229.

[62] C.-M. Ho and L.-S. Huang, "Subharmonics and vortex merging in mixing layers," J. Fluid Mech. **119**, 443–473 (1982).

[63] R. E. Kelly, "On the stability of an inviscid shear layer which is periodic in space and time," J. Fluid Mech. **27**, 657–689 (1967).

[64] P. A. Monkewitz and P. Huerre, "Influence of the velocity ratio on the spatial instability of mixing layers," Phys. Fluids **25**, 1137 (1982).

[65] R. Gerakopulos and S. Yarusevych, "Novel Time-Resolved Pressure Measurements on an Airfoil at a Low Reynolds Number," AIAA J. **50**, 1189–1200 (2012).

[66] R. Parker, "Resonance effects in wake shedding from parallel plates: Some experimental observations," J. Sound Vib. **4**, 62–72 (1966).

[67] R. Parker, "Resonance effects in wake shedding from parallel plates: Calculation of resonant frequencies," J. Sound Vib. **5**, 330–343 (1967).

[68] E. C. Nash, M. V. Lowson, and A. McAlpine, "Boundary-layer instability noise on aerofoils," J. Fluid Mech. **382**, 22–61 (1999).

[69] T. Atobe, M. Tuinstra, and S. Takagi, "Airfoil Tonal Noise Generation in Resonant Environments," Trans. Japan Soc. Aero. Sp. Sci. **52**, 74–80 (2009).

[70] A. Melling, "Tracer particles and seeding for particle image velocimetry," Meas. Sci. Technol. **8**, 1406–1416 (1997).

[71] M. Raffel, C. Willert, S. Wereley, and J. Kompenhans, *Particle Image Velocimetry: A Practical Guide*, 2nd ed. (Springer, 2007).

[72] F. Scarano and M. L. Riethmuller, "Advances in iterative multigrid PIV image processing," Exp. Fluids **29**, S051–S060 (2000).

[73] J. Westerweel and F. Scarano, "Universal outlier detection for PIV data," Exp. Fluids **39**, 1096–1100 (2005).

[74] B. Wieneke, "PIV uncertainty quantification from correlation statistics," Meas. Sci. Technol. **26**, 074002 (2015).

[75] R. J. Moffat, "Describing the uncertainties in experimental results," Exp. Therm. Fluid Sci. **1**, 3–17 (1988).

[76] D. Rodríguez and V. Theofilis, "Structural changes of laminar separation bubbles induced by global linear instability," J. Fluid Mech. **655**, 280–305 (2010).

[77] D. Rodríguez, E. M. Gennaro, and M. P. Juniper, "The two classes of primary modal instability in laminar separation bubbles," J. Fluid Mech. **734**, R4 (2013).

[78] J. Jeong and F. Hussain, "On the identification of a vortex," J. Fluid Mech. **285**, 69–94 (1995).

[79] See Supplemental Material at http://link.aps.org/supplemental/10.1103/PhysRevFluids.4.063903 for movies showing flow development and vortex merging in the separation bubble.

[80] I. Daubechies, *Ten Lect. Wavelets* (Society for Industrial and Applied Mathematics, 1992).

[81] M. S. Howe, *Acoustics of Fluid–Structure Interactions*, edited by G. K. Batchelor, L. B. Freund, S. Leibovich, and V. Tvergaard (Cambridge University Press, Cambridge, 1998).

[82] L. Sirovich, "Turbulence and the Dynamics of Coherent Structures," Q. Appl. Math. **XLV**, 561–590 (1987).

[83] D. Wee, T. Yi, A. Annaswamy, and A. F. Ghoniem, "Self-sustained oscillations and vortex shedding in backward-facing step flows: Simulation and linear instability analysis," Phys. Fluids **16**, 3361–3373 (2004).

[84] B. W. van Oudheusden, F. Scarano, N. P. van Hinsberg, and D. W. Watt, "Phase-resolved characterization of vortex shedding in the near wake of a square-section cylinder at incidence," Exp. Fluids **39**, 86–98 (2005).